

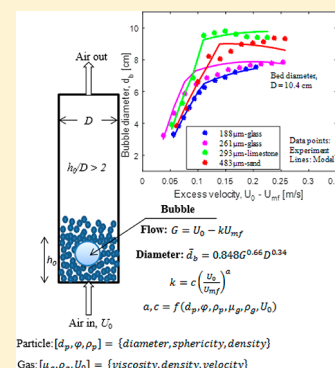
Models for Predicting Average Bubble Diameter and Volumetric Bubble Flux in Deep Fluidized Beds

Cornelius E. Agu,^{*,†} Christoph Pfeifer,[‡] Marianne Eikeland,[†] Lars-Andre Tokheim,[†] and Britt M. E. Moldestad[†]

[†]Department of Process, Energy, and Environmental Technology, University College of Southeast Norway, 3918 Porsgrunn, Norway

[‡]Department of Material Sciences and Process Engineering, University of Natural Resources and Life Sciences, 1190 Vienna, Austria

ABSTRACT: The average bubble diameter and volumetric bubble flux give indications about the overall bed expansion in a fluidized bed. As these properties depend on the particle properties and fluidized bed regime, their accurate predictions have been a challenge. A new set of models for predicting the average bubble properties within the bubbling and slugging regimes in a deep fluidized bed is proposed, where bubble flux is modeled by $G = U_0 - c \left(\frac{U_0}{U_{mf}} \right)^a U_{mf}$, bubble diameter is modeled by $\bar{d}_b = 0.848 G^{0.66} D^{0.34}$ and transition velocity is modeled by $\frac{U_{bs}}{U_{mf}} = 1 + 2.33 U_{mf}^{-0.027} (\varphi^{0.35} c_t^a - 1) \left(\frac{h_0}{D} \right)^{-0.588}$. The models are developed using the information obtained from an experimental setup equipped with a dual-plane electrical capacitance tomography and a porous distributor plate. Although they are empirical, the proposed models are based on the two-phase theory used in describing the bubble flow in a fluidized bed. These models have been validated, and the results show that they can be used to predict the behavior in different regimes at different gas velocities.



1. INTRODUCTION

Due to numerous advantages, fluidized bed technologies have wide industrial applications. To ensure sufficient residence time for the reacting gases, a fluidized bed reactor can be operated in bubbling or nonbubbling regime. Nonbubbling fluidization is also regarded as particulate fluidization, and it is often desired when high gas residence time is required. In the bubbling fluidized bed, there is higher transfer of heat and mass due to a higher degree of solid movement, but this is at the expense of gas residence time. Particle size is among the factors that influence the fluidized bed regimes. For Geldart A particles,¹ a fluidized bed passes through the particulate regime before it begins to bubble when the gas velocity is further increased, whereas for Geldart B particles, which can be fluidized easily, bubbles appear in the bed as soon as the minimum fluidization velocity is exceeded. Mandal et al.² show that a bed of Geldart B particles can exhibit nonbubbling fluidized bed behavior at higher gas velocity when it is formed within the interstitial void space of large and stationary particles. Similar to internals such as vertical tubes and baffles, the large particles serve as bubble breakers, preventing rise and flow of bubbles in the binary beds. In this study, the focus is on the bubbling fluidized beds often applied in small-scale reactors. Designing a bubbling fluidized bed reactor, especially in the preliminary stage, may require a knowledge about the average bed properties. For a given gas velocity, the average bubble diameter and volumetric bubble flux are important parameters that give an indication of bed expansion.

Several correlations^{3–6} found in the literature provide the bubble diameter at any position along the axis of the bed. For a

given superficial gas velocity above the minimum fluidization velocity, these correlations give the same bubble diameter independent of the particle characteristics. This may probably be because most of these models are developed based on the two-phase theory proposed by Toomey and Johnstone.⁷ According to the two-phase theory, the gas velocity in excess of the minimum fluidization velocity constitutes the bubble flow in the bed. On the basis of this assumption, different beds of particles have the same volumetric bubble flux at the same excess gas velocity independent of the particle properties. However, studies of Hillgardt and Werther⁸ and Grace and Cliff⁹ showed that the actual volumetric bubble flux is lower than that given by the two-phase theory. These findings indicate that many of the existing bubble diameter models may not be appropriate for all systems. Moreover, the bubble diameter and volumetric bubble flux at the same excess gas velocity have been observed to vary between different types of particles. Several factors, which include particle shape and size distribution, can be responsible for this deviation.

Accurate prediction of bubble diameter in deep fluidized beds has also been a challenge for most of the available models because they are developed for freely bubbling beds. For a deep bed where there is a possibility of slug flow, none of these models has been found to predict the behavior in the slugging regime. Even though they are developed for freely bubbling

Received: October 22, 2017

Revised: January 30, 2018

Accepted: February 1, 2018

Published: February 1, 2018

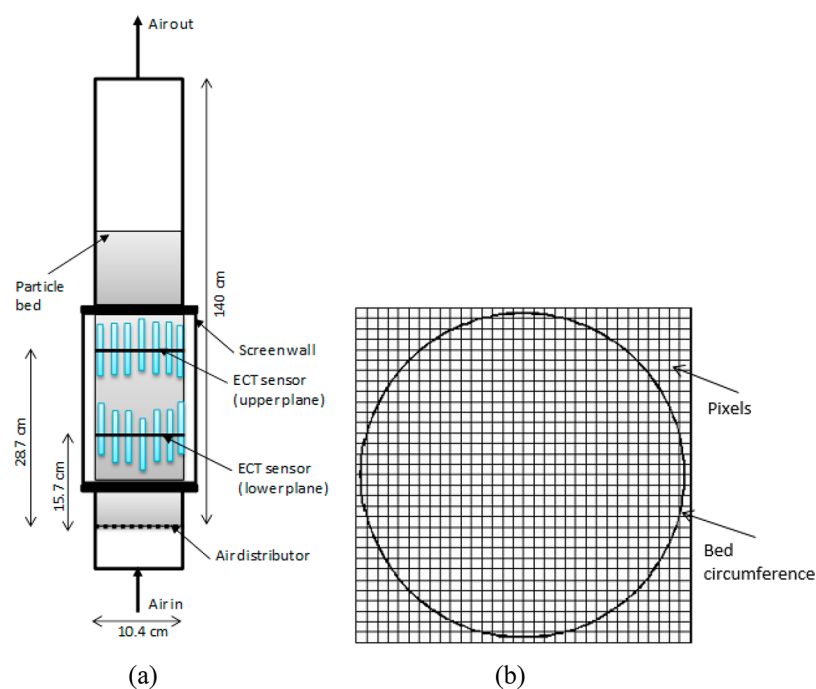


Figure 1. (a) Physical view of a cold fluidized bed with dual-plane ECT sensors for measurement of the solids fraction distribution. (b) Cross section of the bed divided into 812 pixels.

beds, the predictabilities of these different models also differ from one system to another. Karimipour and Pugsley¹⁰ reported that bubble diameters in the beds of Geldart B particles can be best predicted using the models developed by Choi et al.³ and Mori and Wen,⁴ while for Geldart A and D particles, the correlation of Cai et al.¹¹ is best suited. As most of these correlations are either fully empirical or semiempirical, the measurement techniques used to acquire the experimental data for their developments may also influence their accuracies. Although the use of photographic techniques (video imaging) in two-dimensional (2D) beds provides adequate information about the bubble growth, bubble shape and bubble spatial distribution,¹² this information may not be applicable for three-dimensional (3D) beds. Most of the techniques used for 3D systems do not measure the bubble diameter directly. Depending on the technique, the information acquired during the bubble passage is analyzed to obtain the relevant bubble properties such as bubble holdup, bubble size, and bubble rise velocity. Since these properties are inter-related, measurement of any one of them is often used to determine the other properties.¹² X- and γ -ray absorption techniques are widely applied to obtain properties of a single rising bubble.^{5,13,14} For beds with a large diameter, these methods fail to provide accurate bubble properties due to difficulties to identify a particular bubble in the presence of large number of different bubbles. Different types of probes are also employed to measure the bubble properties.^{3,5,15–18} The needle capacitance probes are extensively used^{5,15} despite their low signal-to-noise ratio. In general, the techniques based on the use of conductivity, inductance, and capacitance probes provide information about the local bubble size, but to obtain the average bubble diameter at any cross-section of the bed requires a considerable effort.¹² Being intrusive devices, probes also have the capacities to change the hydrodynamics of their surroundings, thus acquiring false results. Viswanathan and Rao¹² obtained the bubble holdup from pressure measure-

ments, and provided an iterative procedure for determining the bubble diameter by back-calculations using the relevant correlations relating the bubble rise velocity, bubble holdup, and bubble diameter.

The aim of this study is to develop a set of models for obtaining the average bubble volumetric flux and bubble diameter in deep fluidized beds. Farshi et al.¹⁹ highlighted four different ways to compute the average bubble diameter, which is also called the effective diameter. Each of these methods depends on the total bed height, and the simplest of them is by finding the bubble diameter at the middle of the bed. Due to variety of concepts involved, these different methods may give different results. This paper presents models that are independent of the total bed height for obtaining the average bubble diameter and average volumetric bubble flux. The models are based on the analysis of information obtained from an experimental setup equipped with a dual-plane electrical capacitance tomography (ECT). Being a noninvasive technique, a number of researchers^{20–22} have used ECT in their studies to characterize bubbling fluidized beds. ECT sensors provide adequate information about the solids fraction distribution, which can be analyzed to obtain different bubble properties at a given plane in a fluidized bed. In this study, sets of ECT data are acquired and analyzed with different MATLAB codes. From the data analysis, relevant bubble properties are found, which are then used to develop the models for determining the gas velocity at transition between bubbling and slugging regime, the average bubble volumetric flux and the average bubble diameter at different gas velocity. The experimental method used for the data acquisition is presented in the following section, while the details for the proposed model development are given in the subsequent sections.

2. DATA ACQUISITION

2.1. Experimental Setup. In this paper, the experimental setup used to acquire the necessary data consists of a cylindrical

Table 1. Properties of Different Particles Investigated in This Work

| materials | mean particle diameter [μm] | density [kg/m^3] | Geldart group | sphericity [-] | fixed bed solids fraction [-] | minimum fluidization velocity [cm/s] |
|-----------------|--|------------------------------------|---------------|----------------|-------------------------------|--|
| glass beads | 188 | 2500 | B | 1.0 | 0.63 | 4.00 |
| glass beads | 261 | 2500 | B | 1.0 | 0.62 | 8.15 |
| limestone | 293 | 2837 | B | 0.65 | 0.51 | 14.00 |
| sand | 483 | 2650 | B | 0.72 | 0.55 | 17.5 |
| glass | 624 | 2500 | B/D | 1.0 | 0.62 | 23.30 |
| limestone | 697 | 2837 | D | 0.65 | 0.49 | 39.24 |
| molecular sieve | 2170 | 1300 | D | 1.0 | 0.6 | 76.85 |

column of 104 mm internal diameter equipped with a dual-plane ECT sensor as shown in Figure 1. The sensors are located at two different positions: 15.7 and 28.7 cm above the gas distributor. Each sensor consists of 12 electrodes, uniformly distributed around the measurement plane. The cross-section of each sensor is divided into 32×32 square pixels, of which 812 pixels lie within the bed as shown in Figure 1b. Each pixel holds a normalized relative permittivity between 0 and 1. The normalized relative permittivity ϵ_r is a measure of volume fraction of solids in the bed. The volume fraction of particles ϵ_s at any point in the plane is obtained from $\epsilon_s = \epsilon_{s0}\epsilon_r$, where ϵ_{s0} is the fixed bed solids fraction. More detail about this setup can be found in Agu et al.²³

The experiments were conducted using seven different types of particles. The properties and Geldart classification of these particles are given in Table 1. The minimum fluidization velocity of these different particles were obtained from this setup. The particle densities for the different powders were measured with a gas pycnometer and the particle sizes were obtained from the sieve analysis. The average sphericity of the particles is difficult to measure, although the approximate value can be obtained by fitting experimental pressure drop data to a pressure drop model²⁴ such as Carman–Kozeny²⁵ and Ergun²⁶ equations. However, the value of sphericity obtained from this method may differ from one pressure drop equation to another. For the purpose of model development, the sphericity values given in Table 1 correspond to the average of those listed in the literature for the same materials. The initial bed height in each of the experiments lied between 40 and 65 cm. For the Geldart B glass and limestone particles, the experiments were performed with three different initial bed heights, 52, 58, and 64 cm, to obtain the influence of bed height on the fluidized bed behavior.

In the experiments, dry compressed air was used. The air velocity above the minimum fluidization velocity for the different types of particles was varied in the range of 0.05–0.40 m/s. For each air velocity, the images of the solids distribution at the measurement planes were captured. The image data were recorded for 60 s at a frequency of 100 Hz. Figure 2 is an example of the solids fraction distribution obtained during the experiments. The higher values on the figure color bar indicate higher solid concentrations. The flow of bubbles can be observed in the regions where the solid concentration approaches zero. Considering that bubbles contain some amount of solids,²⁴ any region bounded by the solids fraction between 0 and 0.2 is regarded as a bubble in this work. On the basis of this bubble–solid threshold, different bubbles are identified. The bubble properties are calculated using the “image processing toolbox” in MATLAB. The number of pixels occupied by a bubble at any given time is obtained and mapped into the actual bubble projected area using $A_b = A \left(\frac{N_b}{N_{\text{pix}}} \right)$,

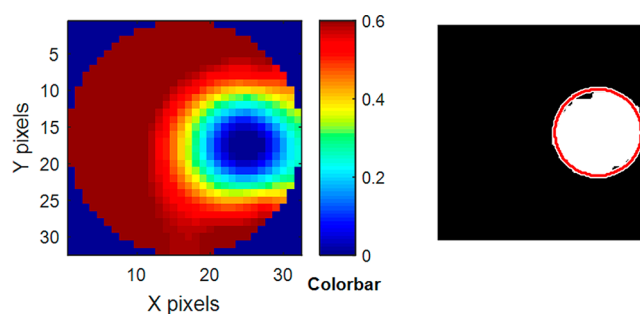


Figure 2. Fluidized bed behavior obtained at the ECT lower plane for the 261 μm glass particles. (a) Distribution of solids where numbers in the color bar give the solids volume fraction. (b) Region occupied by the actual bubble (white) and region defined by approximately spherical bubble (bounded by a red circle).

where A is the cross-sectional area of the bed, N_b is the number of pixels occupied by the bubble, and $N_{\text{pix}} = 812$ is the total number of pixels within the plane. The changes in the values of A_b with time are used to obtain other properties such as bubble frequency and bubble volumetric flow rate as described in the following section.

2.2. Measurement of Bubble Properties. Analysis of the experimental data shows that the passage of bubbles through a given plane is in a regular periodic manner. Figure 3 is the

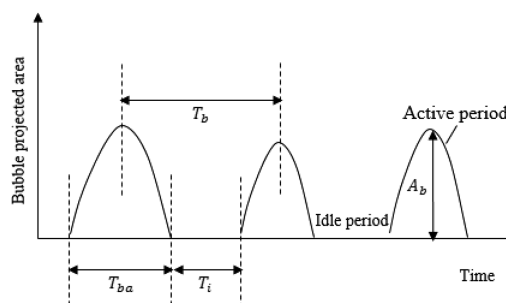


Figure 3. Evolution of bubble-projected area, showing the active and idle periods in a deep bed. Symbols: T_{ba} average active bubble period, T_i average idle period, T_b total bubble period, and A_b average bubble cross-sectional area.

variation of bubble-projected area with time, which is typical for all the beds studied in this work. The projected area increases from zero to a peak value and then decreases to zero as the bubble passes through a given plane. This variation indicates that bubble shape is either spherical or oval. When a bubble first arrives a plane, its projected area is zero. The bubble projected area decreases to zero from a peak value immediately the bubble leaves the plane. The peak of the projected area represents the bubble cross-sectional area through its center.

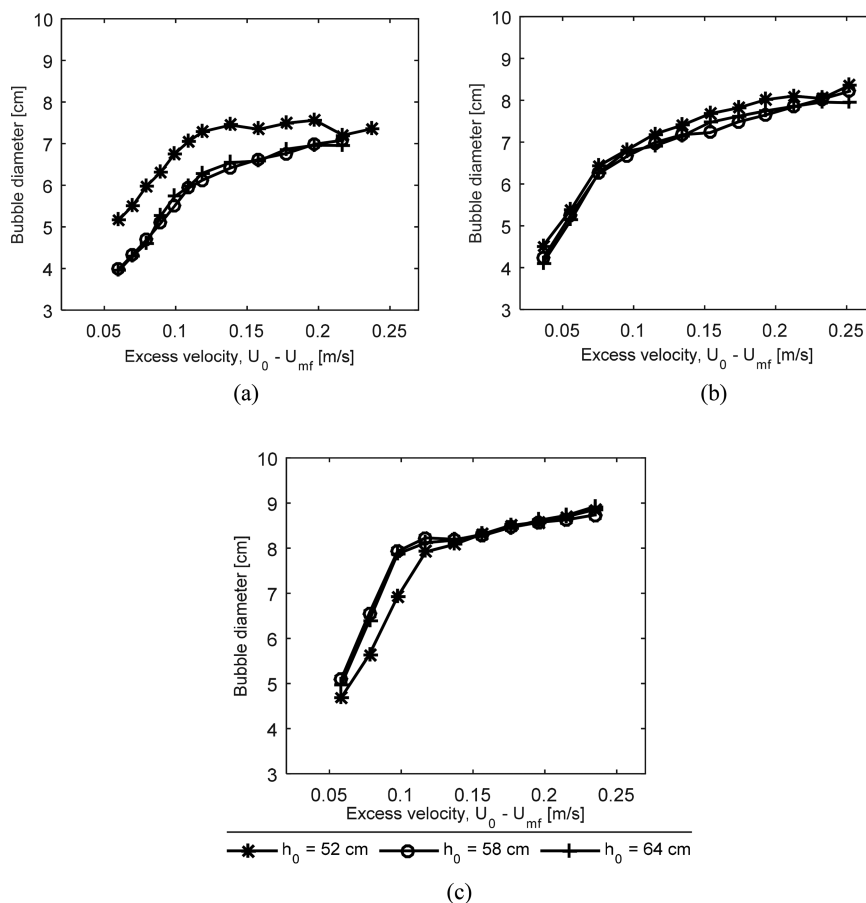


Figure 4. Effect of bed height on the bubble diameters measured at 28.7 cm above the distributor: (a) 188 μm glass particles, (b) 261 μm glass particles, and (c) 293 μm limestone particles.

The time interval between when the bubble arrives and when it completely leaves the plane is described as the active bubble period.

The bubble diameter can be best determined from the bubble equivalent volume.²⁷ In this study, the 2D ECT sensors employed only provide information about the bubble cross-sectional area and none for the bubble height, making it difficult to measure the bubble volume directly. Assuming a spherical bubble, an approximate bubble size can be obtained from the peak of the projected areas. The time-average bubble diameter can therefore be described by

$$d_b = \frac{1}{n} \sum \left(\sqrt{\frac{4A_{b,i}}{\pi}} \right) \tag{1}$$

where n is the number of peaks of the projected areas recorded over the measurement period and $A_{b,i}$ is the peak of the projected areas during the individual bubble passage. The active bubble frequency f_{ba} is obtained as the reciprocal of the active bubble period:

$$f_{ba} = \frac{1}{T_{ba}} \tag{2}$$

$$T_{ba} = \frac{1}{n} \sum T_{bai} \tag{3}$$

Here T_{ba} is the time-average of the individual active bubble periods, T_{bai} . It should be noted that the concept of active bubble period and frequency are introduced in this work, and

that the true bubble period T_b is represented by the sum of the active and idle periods as shown in Figure 3. The true bubble frequency is lower than the active bubble frequency since $T_b > T_{ba}$.

The volumetric bubble flux G is measured by considering the volume of bubble that passes through an observer plane of unit area in a unit time. Considering that the active bubble period is the time for complete bubble passage as shown in Figure 3, the volumetric bubble flux can be expressed as

$$G = \frac{v_b}{AT_{ba}} \tag{4}$$

where v_b is the volume of bubble that passes through a given plane within the time period T_{ba} . For spherical bubbles, $v_b = \frac{\pi}{6}d_b^3$, and eq 4 can be rewritten as

$$G = \frac{\pi}{6A} f_{ba} d_b^3 \tag{5}$$

3. MODEL DEVELOPMENT, RESULTS, AND DISCUSSION

As stated earlier, the proposed models for predicting the average bubble volumetric flux and bubble diameter are independent of initial bed height within the bubbling and slugging regime. This statement is first discussed here.

Figure 4 shows the bubble diameters measured at 28.7 cm above the distributor in different beds of particles: 188 μm glass particles, 261 μm glass particles, and 293 μm limestone

particles. For the beds of 261 μm glass particles, the bubble diameter is independent of the initial bed height at the same gas velocity. For the 293 μm limestone and 188 μm glass particles beds, there are also no differences in the corresponding bubble diameters when the initial bed height is increased from 58 to 64 cm. However, for the height of 52 cm, the bed of 188 μm glass particles shows a significant increase in bubble diameters while that of 293 μm limestone particles shows a decrease in bubble diameters compared with the values recorded at the bed height of 58 cm, although this effect seems to decrease with increasing gas velocity. These results show that the bubble diameter is independent of bed height when the bed height is relatively high. Therefore, the models developed in this section are to be applied in deep beds with large aspect ratios (bed height to bed diameter ratio).

3.1. Model for Average Volumetric Bubble Flux.

According to Grace and Clift,⁹ the volumetric bubble flux can be expressed as

$$G = U_0 - kU_{mf} \quad (6)$$

Equation 6 is a form of modified two-phase theory describing the bubble flow rate in a fluidized bed, where the parameter k accounts for deviation of the theoretical bubble flow rate from the actual bubble volumetric flow rate. The value of k may vary depending on the superficial gas velocity, bed properties and vertical position in the bed.²⁸ In a freely bubbling beds, Choi et al.²⁹ obtained a correlation between the value of k and the gas velocity ratio as given in eq 7, where a and c are constant with values of 0.62 and 1.0, respectively.

$$k = c \left(\frac{U_0}{U_{mf}} \right)^a \quad (7)$$

In the present work, values of k are obtained and analyzed. From the measured volumetric bubble flux, $k = \frac{(U_0 - G)}{U_{mf}}$ can be determined. Figure 5 shows the average values of k against the gas velocity ratios $\frac{U_0}{U_{mf}}$ for four different beds: 483 μm sand, 293 μm limestone, 261 μm glass, and 188 μm glass. In each bed, the trend of variation in k changes as the bed transits from bubbling to slugging regime with increasing gas velocity. The data in the

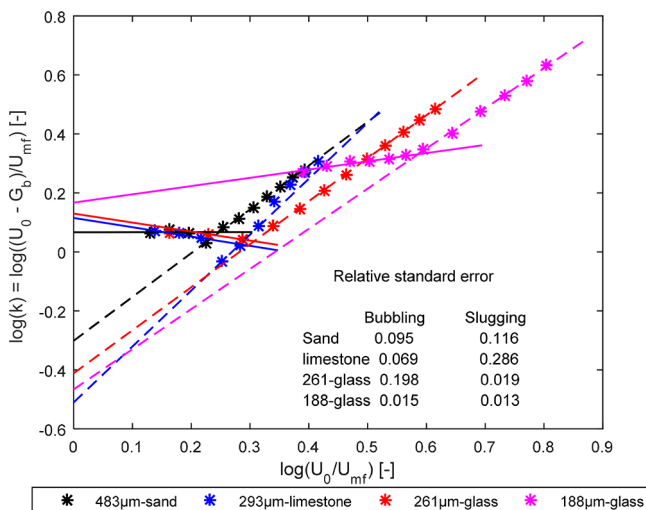


Figure 5. Variation of $k = (U_0 - G)/U_{mf}$ with gas velocity ratio U_0/U_{mf} . Solid lines, bubbling regime; dashed lines, slugging regime.

two different regimes can be fitted with separate straight lines as shown in the figure. The extension of the fitting lines beyond the data points is arbitrary. For example, at the vertical intercept where $\frac{U_0}{U_{mf}} = 1$, slugs are never observed. The value of $\frac{U_0}{U_{mf}} = 1$ gives the minimum possible velocity for a bubble to flow, and depending on the particle size, a bubble may or may not exist at this velocity. However, since the lines are used to describe the behavior in the different regimes, the vertical intercepts as well as the line slopes are essential. Also, as shown in Figure 5, the relative standard error for each of the fitting lines is small, indicating that the data points can be well described by the linear functions.

The slope of each line increases as the flow regime changes from bubbling to slugging. In the bubbling regime, the intercept on the vertical axis is closer to zero for the larger particles, but increases as the particle size decreases. This variation is as expected since smaller particles require significantly higher values of $\frac{U_0}{U_{mf}}$ for the bubble to rise in the beds. In addition, the line slopes in this regime differ between the different beds. The slope decreases between 188 μm glass and limestone and increases thereafter toward the sand particles. This behavior can be attributed to the variation in size and shape between these particles. However, in the slugging regime, sand and glass particles have almost the same line slopes, which differ significantly from that of limestone particles.

On the basis of these linear relationships shown in Figure 5, the expression $k = c \left(\frac{U_0}{U_{mf}} \right)^a$ can be used to describe the behavior in both bubbling and slugging regimes, where a and c are the line slope and the line intercept, respectively. As described above, the values of a and c depend on the particle size, shape, and fluidization regime. Further analysis of these behavior (Figure 5) provides different expressions for values of a and c as given in Table 2. For the slugging regime, the

Table 2. Correlations for the Proposed Model Parameters a and c

| parameters | expressions | validity |
|-----------------|--|---------------------|
| Bubbling Regime | | |
| a | $\varphi^{1.5}(4.168 - 1.389 \log(Ar))$ | $\log(Ar) < 3.5$ |
| | $\varphi^{1.5}(0.329 - 1.156 \times 10^3 Ar^{-0.9})$ | $\log(Ar) \geq 3.5$ |
| c | $(1.321 + 8.161 \times 10^4 Ar^{-1.04})^{0.083}$ | $\log(Ar) > 0$ |
| Slugging Regime | | |
| a | $0.725 + 0.230 \log(Ar)$ | $\log(Ar) < 3.9$ |
| | $1.184 + 8.962 \times 10^4 Ar^{-1.35}$ | $\log(Ar) \geq 3.9$ |
| c | $0.042 + 0.108 \log(Ar)$ | $\log(Ar) < 4.0$ |
| | $(0.978 - 1.964 \times 10^2 Ar^{-0.8})^{4.88}$ | $\log(Ar) \geq 4.0$ |

correlations are based on the beds of 188 μm glass, 293 μm limestone, sand, 697 μm limestone, and the 3D molecular sieves particles. The correlations for the bubbling regime are based on the glass particles (188 and 261 μm), the sand particles and two of the Geldart D particles (697 μm limestone and 2.17 mm molecular sieve particles).

Table 2 shows that the expressions for a and c vary between the bubbling and slugging regimes and that these parameters depend on the particle Archimedes number, $Ar = d_p^3 \rho_g (\rho_p - \rho_g) g / \mu_g^2$, where d_p is the particle diameter, φ is the particle sphericity, ρ_p is the particle density, and g is the acceleration

due to gravity. ρ_g and μ_g are the gas density and dynamic viscosity, respectively.

3.1.1. Validation of the Proposed Model for Volumetric Bubble Flux. Using the expressions for the parameters a and c as given in Table 2, the average volumetric bubble flux in deep fluidized beds can be obtained from

$$G = U_0 - c \left(\frac{U_0}{U_{mf}} \right)^a U_{mf} \quad (8)$$

Figure 6 compares the average volumetric bubble flux obtained from eq 8 with the experimental data. As shown in the figure,

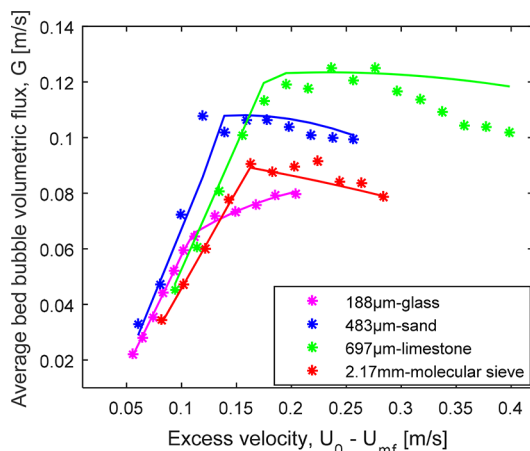


Figure 6. Computed average volumetric bubble flux based on $G = U_0 - c \left(\frac{U_0}{U_{mf}} \right)^a U_{mf}$ (lines) compared with the experimental data (stars) used in the model development.

these results are for the particles used in developing the models in Table 2. Quantitatively, it can be seen that the model results are in good agreement with the experimental data. The transition from bubbling to slugging regimes are well-captured, and the trends of the bubble flux in both regimes correspond with those of the experiments. Figure 7 shows the computed average volumetric bubble flux against the gas excess velocity

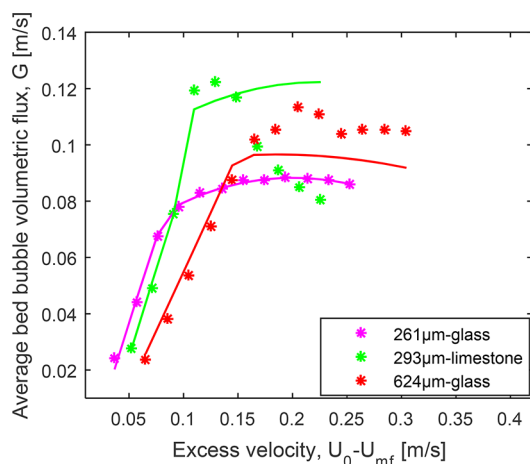


Figure 7. Computed results (lines) based on the proposed model $G = U_0 - c \left(\frac{U_0}{U_{mf}} \right)^a U_{mf}$ compared with the experimental data (stars) from different beds.

for other sets of particles also studied in this work. It can be seen that the model prediction is also in good agreement with the experimental data within the given range of gas velocities.

3.2. Model for Gas Velocity at Bubble to Slug Transition. To apply the models in Table 2 successfully at any given gas velocity, a model at the boundary between the bubbling and slugging regimes is required. Different bubble–slug transition models are available in the literature.^{30–33} The transition models provide the velocity at the onset of slugging. Among the available models, the Baeyens and Geldart³⁰ model is commonly used.

$$U_{ms} = U_{mf} + 0.16(1.3D^{0.175} - h_{mf})^2 + 0.07(gD)^{0.5} \quad (9)$$

The Baeyens and Geldart³⁰ correlation (eq 9) shows that the minimum gas velocity required for a slug to flow in a fluidized bed depends on the particle minimum fluidization velocity, the bed height, and the bed diameter, but the excess velocity $U_{ms} - U_{mf}$ is independent of the fluid and particle properties except where h_{mf} changes with these properties. In this section, a model where $U_{ms} - U_{mf}$ is fully dependent on fluid and particle properties is developed.

As shown in Figure 5, the transition from bubbling to slugging regime occurs at the point of intersection between the two different regime lines. At the intersection, the values of k from the two regimes are the same:

$$c_b \left(\frac{U_{ms}}{U_{mf}} \right)^{a_b} = c_s \left(\frac{U_{ms}}{U_{mf}} \right)^{a_s} \quad (10)$$

Here, a_b and a_s are the corresponding values of a in the bubbling and slugging regimes, c_b and c_s are the respective values of c , and U_{ms} is the superficial gas velocity at the transition. With the values of a and c known in the respective regime, eq 10 can be simplified:

$$\frac{U_{ms}}{U_{mf}} = c_t^{a_t} \quad (11)$$

where $c_t = c_b/c_s$ and $a_t = 1/(a_s - a_b)$.

Figure 8 compares the transition velocity ratios computed from eq 11 with those obtained in the experiment for the different powders. For the spherical particles, the results show that the computed data agree very well with the experimental data. The results differ significantly when the particles are nonspherical. This indicates that at the onset of slugging

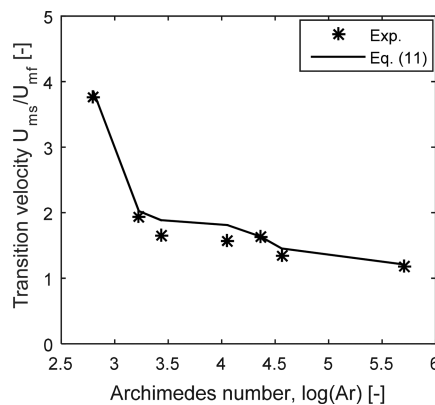


Figure 8. Computed values of gas velocity ratio at the transition from bubbling to slugging regime for different particles using eq 11.

regime, particle shape plays a significant role. In Dimattia et al.,³⁴ the minimum slugging velocity is also reported to depend on the particle sphericity. Therefore, eq 11 can be modified to account for the influence of particle sphericity at the transition.

By introducing a factor of $\varphi^{0.35}$ in eq 11, the errors associated with the computed values of $\frac{U_{ms}}{U_{mf}}$ for the nonspherical particles are minimized.

$$\frac{U_{ms}}{U_{mf}} = \varphi^{0.35} c_t^{a_t} \quad (12)$$

Contrary to the Baeyens and Geldart model, the results from eq 12 are independent of the bed height and bed diameter. This shows that the transition velocity described by this model can be accurate when the bed is relatively deep, that is, where $\frac{h_0}{D} \geq 4$. To be able to utilize eq 12 in beds with smaller aspect ratios, some modifications are needed.

Agu et al.²³ show that the onset of slugging depends on the bed height especially in the bed of smaller particles, and as given by eq 9, this in general should depend on both h_0 and D .

Figure 9 shows the ratio, $\frac{U_{ms}/U_{mf}-1}{(\varphi^{0.35}c_t^{a_t}-1)U_{mf}}$, computed against the

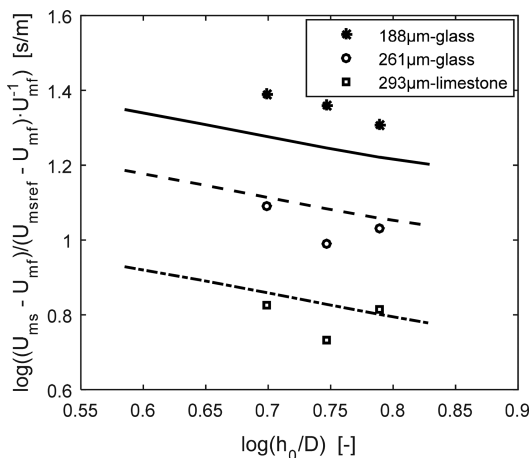


Figure 9. Variation of normalized gas velocity at slugging with bed height. Data points: experiment; lines: Baeyens and Geldart model, eq 9.

bed aspect ratio $\frac{h_0}{D}$ for the different beds: 188 μm glass, 261 μm glass, and 293 μm limestone particles. For the bed of 188 μm glass particles, the experimental data show a continuous decrease in the value of $\frac{U_{ms}/U_{mf}-1}{(\varphi^{0.35}c_t^{a_t}-1)U_{mf}}$ with an increase in $\frac{h_0}{D}$,

but for the two larger particle beds, some degrees of scatter can be observed. However, the results from the Baeyens and Geldart model suggests that the variation of this normalized slug velocity ratio with $\frac{h_0}{D}$ is linear with a constant slope when

$\frac{h_0}{D} < 6.5$ for all the beds. On the basis of this linearity, the following relationship can be derived:

$$\frac{U_{ms}/U_{mf}-1}{(\varphi^{0.35}c_t^{a_t}-1)U_{mf}} = \beta \left(\frac{h_0}{D}\right)^\alpha \quad (13)$$

Here, α is the slope of the line, taken to be constant for all the beds, and β is the intercept on the vertical axis, which decreases with increasing particle size as can be seen in Figure 9.

Figure 10 shows that the three sets of the experimental data can be fitted with different straight lines of the same slope. It

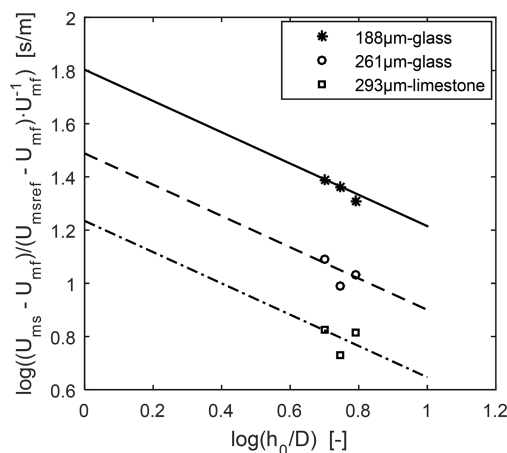


Figure 10. Normalized minimum gas velocity for slugging fitted with constant slope lines.

can be seen clearly that as the particle size increases, the degree of data scatter increases. Dimattia et al.³⁴ also reported a similar scatter variation. The scatter variation indicates that the dependency of the minimum slugging velocity on the bed height may be insignificant when the particle size is large. The slope of each line in Figure 10 is $\alpha = -0.588$. The value of the intercept β is found to depend on the particle minimum fluidization velocity by the expression $\beta = \gamma U_{mf}^\theta$ where $\gamma = 2.33$ and $\theta = -1.027$. From these results, the onset of slugging velocity can be obtained as a function of bed aspect ratio as described by eq 14.

$$\frac{U_{ms}}{U_{mf}} = 1 + 2.33 U_{mf}^{-0.027} (\varphi^{0.35} c_t^{a_t} - 1) \left(\frac{h_0}{D}\right)^{-0.588}; \quad 1.5 < \frac{h_0}{D} < 7.2 \quad (14)$$

The coefficient $U_{mf}^{-0.027}$ in eq 14 accounts for the bed expansion above the height at fixed state during the transition. The bed height expansion is also accounted for in the Baeyens and Geldart model by replacing h_0 with h_{mf} . Note that in both eqs 9 and 14, U_{mf} is measured in m/s. Equations 14 and 9 agree very well within the aspect ratio range of 1.5–7.2, and this is taken as the range of validity of this model until further verification is obtained.

3.2.1. Validation of Proposed Model for Onset of Slugging Regime. Equation 14 shows that both U_{ms} and $U_{ms} - U_{mf}$ depend on the fluid and particle properties. This makes the model more robust to predict the onset of slugging velocity in different systems with varying operating conditions, including temperature and pressure. However, reliability of this model also depends on its performance when compared with results from other setups or correlations.

Figure 11 compares the minimum slugging velocity computed from eq 14 with those obtained in the experiments reported by Singh and Roy.³⁵ The values based on the Baeyens and Geldart model are also shown for comparison. The bed height at minimum fluidization condition, $h_{mf} = \frac{\epsilon_{s0} h_0}{1 - \epsilon_{mf}}$, used in eq 9 is based on the average bed height $h_0 = 55$ cm characterizing the present work. The values of solids fraction ϵ_{s0} in fixed state are given in Singh and Roy³⁶ for the same set of particles. The void fractions at minimum fluidization ϵ_{mf} are

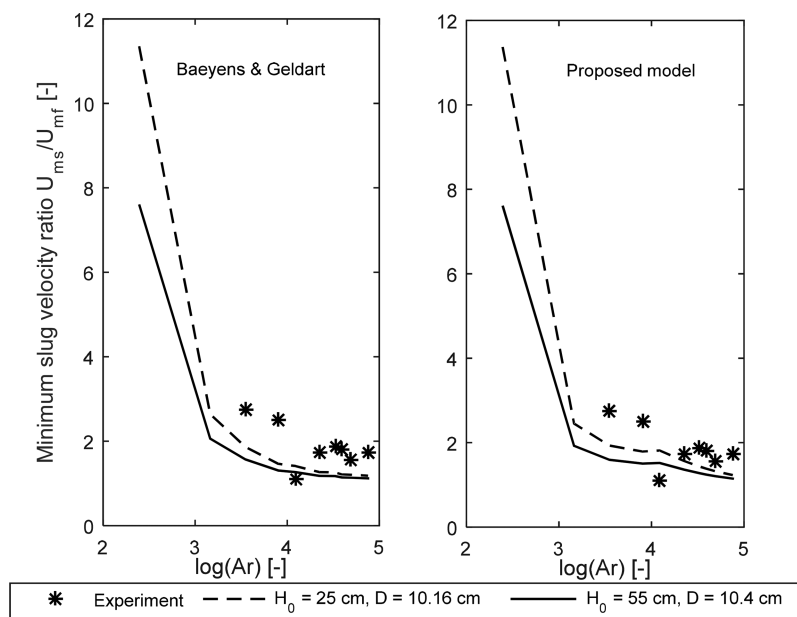


Figure 11. Computed minimum gas velocity for slug flow at different bed heights and bed diameters.

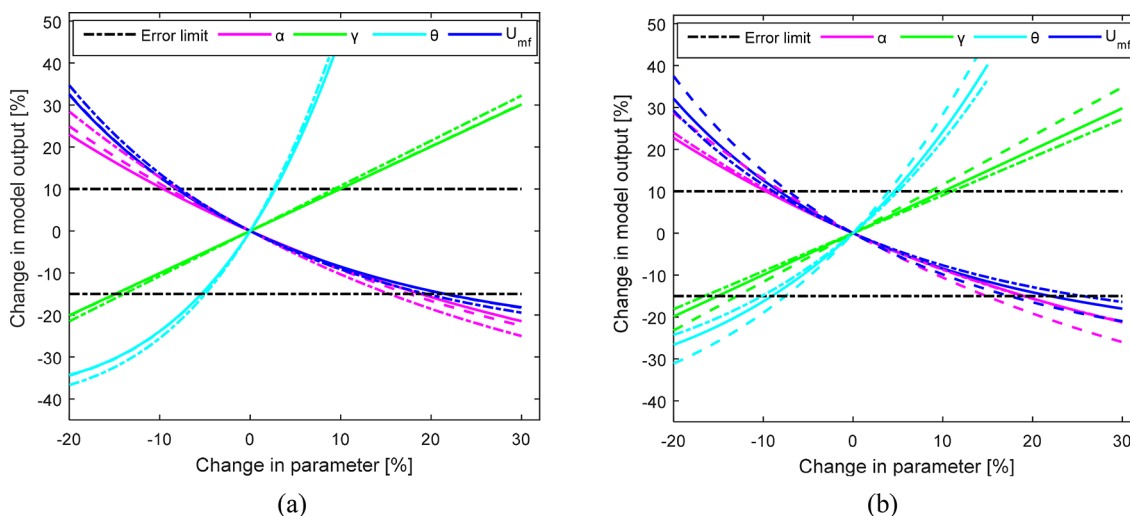


Figure 12. Response of the model $R = \gamma U_{mf}^{\theta} \left(\frac{h_0}{D}\right)^{\alpha}$ for changes in the model parameters at different bed heights. (a) 188 μm glass particles (b) 293 μm limestone particles. Colored lines: $\frac{h_0}{D} = 5.0$ (solid), $\frac{h_0}{D} = 5.6$ (dashed), and $\frac{h_0}{D} = 6.2$ (dotted).

obtained according to Wen and Yu³⁷ based on a sphericity of 0.70 for all the powders. As shown in Figure 11, the proposed model, eq 14 agrees very well with the Baeyens and Geldart model, and the results from both models are in good agreement with the experimental data.

With a different bed height, $h_0 = 25$ cm, and the bed diameter $D = 10.16$ cm reported in Singh and Roy,³⁵ eqs 9 and 14 also agree very well with each other. Compared with eq 9, the proposed model responds very well to the variations in the bed height to bed diameter ratio. The results from both models also show that the effect of bed height is insignificant when increasing the particle size.

3.2.2. Sensitivity of the Model, Equation 14, to the Fitting Parameters α , γ , θ , and U_{mf} . Although the results presented in Figure 11 show that the proposed bubble-slug transition model can predict the onset of slugging regime with good accuracy, the model validity depends on the particle size due to

uncertainty in U_{mf} measurement. In Figure 10, the slopes of the actual lines that can fit separately the data from the three different sets of particles differ from the average value, -0.588 used in the proposed model. The actual intercept of each line also differs from that given by the correlation $\beta = 2.33U_{mf}^{-1.027}$ following the deviation in the corresponding line slope. Due to these deviations, the maximum error associated with the right-hand side of eq 13, $R = \gamma U_{mf}^{\theta} \left(\frac{h_0}{D}\right)^{\alpha}$, lies between -15 and $+10\%$ for all the bed heights. It should be noted that changes in the model parameters α , γ , θ , and U_{mf} from their base values may cause a significant change in the model maximum error. On the basis of this, it will be interesting to check the model sensitivity to these parameters within a possible range of changes.

Figure 12 shows how the model responds to small changes in any of the four parameters. These results show that the model

sensitivity is not affected by changes in the bed aspect ratio for changes in any of the parameters within $\pm 10\%$. For the changes in the parameters α , γ , and U_{mf} , the sensitivity is independent of the bed particles within the $\pm 10\%$ changes. Any slight increase in the parameter θ from the nominal value results in a rapid increase in the model output, although this effect seems to decrease with an increase in the particle size. Hence, due to this high sensitivity, the nominal value $\theta = -1.027$, should be maintained in the model.

As can be seen, a change in α within $\pm 15\%$ has the same effect on the model output as the same change in U_{mf} . Within $\pm 10\%$, a change in γ has the same magnitude, but the opposite effect as an equal change in α or U_{mf} . This means that any change applied to α should be applied to γ to minimize the model error. Since U_{mf} is also a variable in the model, it follows that the value of γ can be varied from the base value according to the uncertainty in measurement or estimation of U_{mf} .

3.3. Model for Average Bubble Diameter. As shown in Figure 3, the active bubble frequency depends on the bubble size. As the bubble size increases, the time taken by the bubble to pass through a given plane increases. Figure 13 shows how

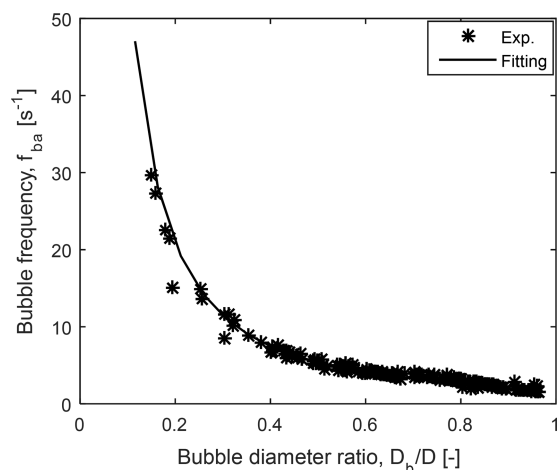


Figure 13. Relationship between the active bubbling frequency and bubble diameter.

the bubble frequency changes with the bubble diameter. The plotted data are obtained from nine different beds of three different types of particles, 188 μm glass, 261 μm glass, and 293 μm limestone, with three different bed heights, 52, 58, and 64 cm. The plot includes all the data obtained from both planes (15.7 and 28.7 cm above the distributor) for each bed. The result indicates that the relationship between the bubble frequency and the bubble diameter is independent of bed height and can be described by a curve with the following function:

$$f_{ba} = 1.927 \left(\frac{D}{d_b} \right)^{1.48} \tag{15}$$

Equation 15 shows that when the bubble diameter is as large as the bed diameter, the active bubble frequency is reduced to 1.93 s^{-1} .

With eq 15, the volumetric bubble flux described by eq 5 can be written as

$$G = 0.321 \frac{\pi}{A} \left(\frac{D}{d_b} \right)^{1.48} d_b^3 \tag{16}$$

Substituting $\frac{\pi}{4} D^2$ for A , eq 16 can be simplified to

$$G = m \left(\frac{d_b}{D} \right)^{1.52} D \tag{17}$$

where m is a constant with a value of 1.285 s^{-1} . Keeping the units of d_b and D the same, the unit of G is thus m/s , cm/s , or mm/s depending on what unit assigned to the bed diameter, D .

The results from eq 17 are compared with the experimental data as shown in Figure 14. The average bubble diameters used in these results are those obtained from the experiments with the different types of particles. As can be seen in Figure 14a, the model predicts the behavior in the different beds with a reasonable accuracy. For the beds of particles shown in Figure 14b, the model accuracies are as good as those obtained from the three beds used in the model development, particularly in the bubbling regime. Moreover, the results show that the model

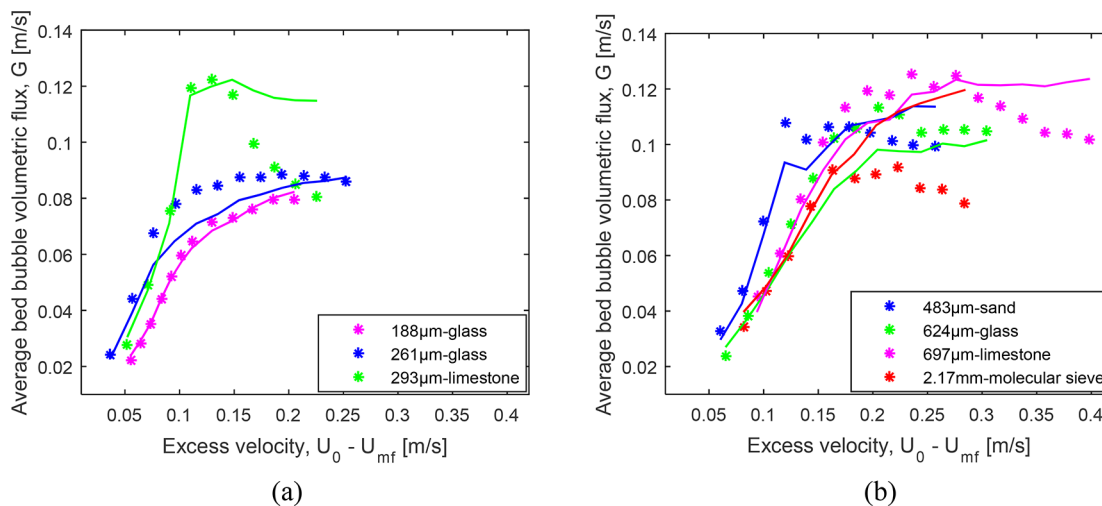


Figure 14. Computed average volumetric bubble flux based on $G = m \left(\frac{d_b}{D} \right)^{1.52} D$ (a) Comparison with data used in the model development. (b) Comparison with data from other different beds.

predicts well the similar behavior observed in the different beds of the same material.

Since the results from both models, eqs 8 and 17, agree very well with the experimental data, a combination of these models can be used to obtain the average bubble diameter in deep fluidized beds at different gas velocities. Assuming that all the bubbles passing over a given bed at a given gas velocity is represented by a single bubble with average diameter \bar{d}_b , a combination of eqs 8 and 17 gives

$$U_0 - c \left(\frac{U_0}{U_{mf}} \right)^a U_{mf} = 1.285 \left(\frac{\bar{d}_b}{D} \right)^{1.52} D \quad (18)$$

Recasting eq 18, the model for average bubble diameter is given by

$$\bar{d}_b = 0.848 \left(U_0 - c \left(\frac{U_0}{U_{mf}} \right)^a U_{mf} \right)^{0.66} D^{0.34} \quad (19)$$

3.3.1. Validation of the Proposed Model for Average Bubble Diameter. For a given gas velocity, the average bubble diameter in a deep fluidized bed can be predicted using eq 19. The unit of gas velocity in this empirical model must be in “per second” and must correspond to any unit assigned to the bed diameter.

To validate this model, the computed average bubble diameters for different beds of particles are compared with the experimental data as shown in Figure 15. These results are

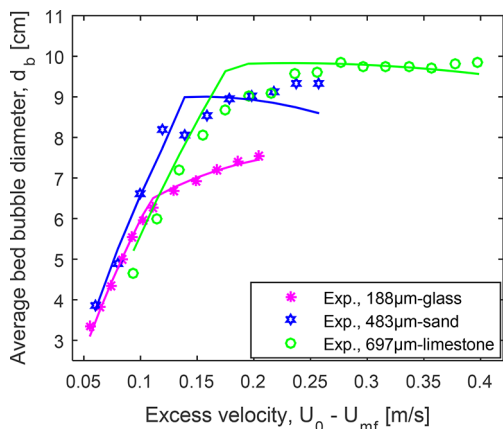


Figure 15. Computed average bubble diameter based on the proposed model $\bar{d}_b = 0.848 \left(U_0 - c \left(\frac{U_0}{U_{mf}} \right)^a U_{mf} \right)^{0.66} D^{0.34}$ compared with the experimental data used in the model development.

based on the set of particles used in formulating the model. The results show that a strong agreement exists between the model and the experimental data within the range of gas velocities shown.

Further validation of this model for average bubble diameter is obtained by comparing its results with those from the existing models. In this case, the models proposed by Choi et al.³ and Mori and Wen⁴ are considered since both models are widely applied in predicting the bubble diameters. The Choi et al. and Mori and Wen models are as described in eqs 20 and 21, respectively.

$$(U_0 - U_{mf})[d_b - d_{b0} - 1.132h] + 0.474g^{0.5}(d_b^{1.5} - d_{b0}^{1.5}) = 0$$

$$d_{b0} = \frac{1.63}{g^{0.2}} [A_c (U_0 - U_{mf})]^{0.4} \quad (20)$$

$$d_b = 0.652 [A(U_0 - U_{mf})]^{0.4} - (0.652 [A(U_0 - U_{mf})]^{0.4} - d_{b0}) \exp\left(-0.3 \frac{h}{D}\right)$$

$$d_{b0} = 0.00376 (U_0 - U_{mf})^2 \quad (21)$$

Here, h [cm] is a vertical position in the fluidized bed, A_c [cm²] is the catchment area described in Darton et al.,⁵ g is in [cm/s²], and U_0 and U_{mf} are in [cm/s]. The bed average bubble diameters based on these models, eqs 20 and 21, are obtained by integration taken between the two measurement planes, 15.7 and 28.7 cm above the gas distributor.

The results from these three models, the present work, the Choi et al.³ model, and the Mori and Wen⁴ models, are shown in Figure 16 for three different beds of particles. The figure

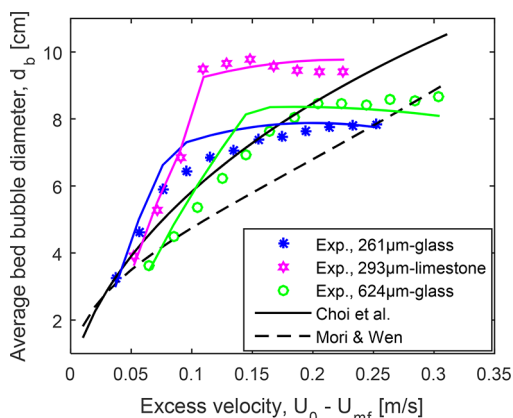


Figure 16. Predictability of the proposed model $\bar{d}_b = 0.848 \left(U_0 - c \left(\frac{U_0}{U_{mf}} \right)^a U_{mf} \right)^{0.66} D^{0.34}$ compared with those of existing models eqs 20 and 21.

shows that the bubble diameters computed with the present model agree very well with the experimental data in all the beds. Each of the Choi et al. and Mori and Wen models predicts the same bubble diameter in the different beds at the same excess gas velocity, $U_0 - U_{mf}$. Within the range of the excess gas velocities shown, the results from the Choi et al. model are closer to the experimental data if averaged compared with those from the Mori and Wen model. While neither Choi et al. nor Mori and Wen model predicts the behavior in the slugging regime, the present model reasonably predicts this behavior. This ability to predict the bubble diameters in different regimes of the deep fluidized beds makes the present model superior to these two other models previously described in the literature.

4. SUMMARY OF THE PROPOSED MODELS

The models developed in this paper for predicting the average volumetric bubble flux, the average bubble diameter, and gas velocity of transition from the bubbling to the slugging are summarized in Table 3. The main assumption of these models is that within the bubbling or the slugging regime the average

Table 3. Proposed Models for Average Bubble Flux, Bubble Diameter, and Bubble to Slug Transition Velocity

| fluidized bed parameter | model |
|---|---|
| volumetric bubble flux | $G = U_0 - c \left(\frac{U_0}{U_{mf}} \right)^a U_{mf}$ |
| bubble diameter | $\bar{d}_b = 0.848 \left(U_0 - c \left(\frac{U_0}{U_{mf}} \right)^a U_{mf} \right)^{0.66} D^{0.34}$ |
| gas velocity at bubble to slug transition | $\frac{U_{ms}}{U_{mf}} = 1 + 2.33 U_{mf}^{-0.027} (\varphi^{0.35} c_t^{a_t} - 1) \left(\frac{h_0}{D} \right)^{-0.588}$ |

volumetric bubble flux and bubble diameter are independent of the initial bed height, h_0 . However, the expressions for the transition velocity indicates that the bed height is an important parameter for determining the regime of operation.

The dependency of the model parameters a and c on the particle and fluid properties makes it possible for the model to predict unique bubble diameter in fluidized beds of different particles with the same excess gas velocity, $U_0 - U_{mf}$. It should be noted that the expressions for G and \bar{d}_b are discontinuous over the entire range of gas velocity $1 < \frac{U_{bs}}{U_{mf}} < \frac{U_0}{U_{mf}}$. The discontinuity over this velocity range is due to the expressions for a and c that are different in the two different regimes. However, within each of the regimes, $1 < \frac{U_0}{U_{mf}} < \frac{U_{bs}}{U_{mf}}$ and $\frac{U_0}{U_{mf}} > \frac{U_{bs}}{U_{mf}}$, the expressions for G and \bar{d}_b are continuous and differentiable.

5. CONCLUSIONS

A fluidized bed can be operated in bubbling or nonbubbling regime depending on the Geldart class of the bed particles. For a bubbling fluidized bed, the bubble properties also depend on the particle properties and fluidized bed regime (freely bubbling or slugging), making their accurate predictions a challenge. This paper presents a set of new models for predicting the average volumetric bubble flux, average bubble diameter and gas velocity at the transition between bubbling and slugging regimes in deep fluidized beds:

Bubble flux:

$$G = U_0 - c \left(\frac{U_0}{U_{mf}} \right)^a U_{mf}$$

Bubble diameter:

$$\bar{d}_b = 0.848 G^{0.66} D^{0.34}$$

Transition velocity:

$$\frac{U_{bs}}{U_{mf}} = 1 + 2.33 U_{mf}^{-0.027} (\varphi^{0.35} c_t^{a_t} - 1) \left(\frac{h_0}{D} \right)^{-0.588}$$

The model parameters a , c , a_t , and c_t depend on the fluid and particle properties, and their correlations with these properties are also presented in this paper. In the slugging regime where $\frac{U_0}{U_{mf}} > \frac{U_{bs}}{U_{mf}}$, the same models are applied but with different correlations for the parameters a and c .

These models are developed based on the analysis of data obtained from a cylindrical setup equipped with a dual-plane electrical capacitance tomography. Although the models are empirical, they are also based on the two-phase theory used in describing the bubble flow in fluidized beds.

These models have been tested with different types of particles having mean diameters in the range of 130–2200 μm , and their results are consistent with different experimental data. The models capture the behavior in different regimes of deep fluidized beds at increasing gas velocity. The dependency of the model for average bubble diameter on the bed diameter increases its applicability for design purposes. However, these models require further validation with experimental data based on different measurement techniques as well as bed height to diameter ratio less than 4.

AUTHOR INFORMATION

Corresponding Author

*E-mail: cornelius.e.agu@usn.no.

ORCID

Cornelius E. Agu: 0000-0002-5339-9794

Notes

The authors declare no competing financial interest.

NOMENCLATURE

| | |
|-----------|---|
| A | bed cross-sectional area, m^2 |
| Ar | dimensionless particle Archimedes number |
| a | dimensionless fitting index |
| c | dimensionless fitting coefficient |
| D | bed diameter, m |
| d | diameter, m |
| \bar{d} | average diameter, m |
| f | frequency, s^{-1} |
| G | volumetric bubble flux, m/s |
| g | acceleration due to gravity, m/s^2 |
| gas | |
| h | vertical position in the bed, m |
| h_0 | initial bed height, m |
| i | index |
| k | dimensionless two-phase bubble flow deviation coefficient |
| log | logarithm function to base 10 |
| m | dimensionless model coefficient |
| N, n | numbers |
| R | right-hand-side of a model |
| T | period, s |
| U | superficial gas velocity, m/s |
| v | volume, m^3 |

Greek Symbols

| | |
|--------------|---|
| α | dimensionless fitting index |
| β | fitting coefficient, s/m |
| ϵ | dimensionless void fraction |
| ϵ_s | dimensionless solids fraction |
| θ | dimensionless fitting index |
| ρ | density, kg/m^3 |
| φ | dimensionless particle sphericity |
| μ | dynamic viscosity, $\text{Pa}\cdot\text{s}$ |
| γ | fitting coefficient, $(\text{m/s}) \theta^{-1}$ |

Subscripts

| | |
|-----|---|
| b | bubble |
| ba | active bubble |
| bs | bubble to slug transition |
| g | acceleration due to gravity, m/s^2 |
| gas | |
| p | particle |
| s | solid |
| t | transition |

0 (zero) initial state or entry position

■ REFERENCES

- (1) Geldart, D. Types of Gas Fluidization. *Powder Technol.* **1973**, *7*, 285.
- (2) Mandal, D.; Vinjamur, M.; Sathiyamoorthy, D. Hydrodynamics of Beds of Small Particles in the Voids of Coarse Particles. *Powder Technol.* **2013**, *235*, 256.
- (3) Choi, J. H.; Son, J. E.; Kim, S. D. Bubble Size and Frequency in Gas Fluidized Beds. *J. Chem. Eng. Jpn.* **1988**, *21*, 171.
- (4) Mori, S.; Wen, C. Y. Estimation of Bubble Diameter in Gaseous Fluidized Beds. *AIChE J.* **1975**, *21*, 109.
- (5) Darton, R. C.; La Nauze, R. D.; Davidson, J. F.; Harrison, D. Bubble Growth due to Coalescence in Fluidized Beds. *Trans. Inst. Chem. Eng.* **1977**, *55*, 274.
- (6) Cranfield, R. R.; Geldart, D. Large Particle Fluidization. *Chem. Eng. Sci.* **1974**, *29*, 935.
- (7) Toomey, R. D.; Johnstone, H. F. Gaseous Fluidization of Solid Particles. *Chem. Eng. Prog.* **1952**, *48*, 220.
- (8) Hillgardt, K.; Werther, J. Local Bubble Gas Hold-up and Expansion of Gas/solid Fluidized Beds. *Ger. Chem. Eng.* **1986**, *9*, 215.
- (9) Grace, J. R.; Clift, R. On the Two-phase Theory of Fluidization. *Chem. Eng. Sci.* **1974**, *29*, 327.
- (10) Karimipour, S.; Pugsley, T. A Critical Evaluation of Literature Correlations for Predicting Bubble Size and Velocity in Gas-solid Fluidized Beds - A review. *Powder Technol.* **2011**, *205*, 1.
- (11) Cai, P.; Schiavetti, M.; De Michele, G.; Grazzini, G. C.; Miccio, M. Quantitative Estimation of Bubble Size in PFBC. *Powder Technol.* **1994**, *80*, 99.
- (12) Viswanathan, K.; Rao, D. S. Measurement of Bubble Size in Fluidized Beds. *Ind. Eng. Chem. Process Des. Dev.* **1984**, *23*, 573.
- (13) Rowe, P. N. Prediction of Bubble Size in a Gas Fluidized Bed. *Chem. Eng. Sci.* **1976**, *31*, 285.
- (14) Rowe, P. N.; Everett, D. J. Fluidized Bed Bubbles Viewed by X-rays. *Trans. Inst. Chem. Eng.* **1972**, *50*, 42.
- (15) Werther, J. Effect of Gas Distributor on the Hydrodynamics of Gas Fluidized Beds. *Ger. Chem. Eng.* **1978**, *1*, 66.
- (16) Davidson, J. F.; Harrison, D. *Fluidized Particles*; Cambridge University Press: London, 1963.
- (17) Yasui, G.; Johanson, L. N. Characteristics of Gas Pockets in Fluidized Beds. *AIChE J.* **1958**, *4*, 445.
- (18) Burgess, J. M.; Calderbank, P. H. The Measurement of Bubble Properties in Two-phase Dispersions-III: Bubble Properties in a Freely Bubbling Fluidized-bed. *Chem. Eng. Sci.* **1975**, *30*, 1511.
- (19) Farshi, A.; Javaherzadeh, H.; Hamzavi-Abedi, M. A. An Investigation of the Effect of Bubble Diameter on the Performance of Gas-solid Fluidized Bed Reactor and Two-phase Modelling of Bubbling Fluidized Bed Reactor in Melamine Production. *Pet. Coal* **2008**, *50*, 11.
- (20) Chandrasekera, T. C.; Li, Y.; Moody, D.; Schnellmann, M. A.; Dennis, J. S.; Holland, D. J. Measurement of Bubble Size in Fluidized Beds Using Electrical Capacitance Tomography. *Chem. Eng. Sci.* **2015**, *126*, 679.
- (21) Wang, H.; Yang, W.; Dyakowski, T.; Liu, S. Study of Bubbling and Slugging Fluidized Beds by Simulation and ECT. *AIChE J.* **2006**, *52*, 3078.
- (22) Makkawi, Y. T.; Wright, P. C. Electrical Capacitance Tomography for Conventional Fluidized Bed Measurements- Remarks on the Measuring Technique. *Powder Technol.* **2004**, *148*, 142.
- (23) Agu, C. E.; Tokheim, L.-A.; Eikeland, M.; Moldestad, B. M. E. Determination of Onset of Bubbling and Slugging in a Fluidized Bed Using a Dual-plane Electrical Capacitance Tomography System. *Chem. Eng. J.* **2017**, *328*, 997.
- (24) Kunii, D.; Levenspiel, O. *Fluidization Engineering*, 2nd ed.; Butterworth-Heinemann: Boston, MA, 1991.
- (25) Carman, P. C. Fluid Flow through Granular Beds. *Trans. Inst. Chem. Eng.* **1937**, *15*, 150.
- (26) Ergun, S. Fluid Flow through Packed Column. *Chem. Eng. Prog.* **1952**, *48*, 89.
- (27) Verma, V.; Padding, J. T.; Deen, N. G.; Kuipers, J. A. M. Effect of Bed Size on Hydrodynamics in 3-D Gas-solid Fluidized Beds. *AIChE J.* **2015**, *61*, 1492.
- (28) Yang, W. C. *Handbook of Fluidization and Fluid-Particle Systems*; Marcel Dekker, Inc.: New York, 2003.
- (29) Choi, J. H.; Son, J. E.; Kim, S. D. Generalized Model for Bubble Size and Frequency in Gas-fluidized Beds. *Ind. Eng. Chem. Res.* **1998**, *37*, 2559.
- (30) Baeyens, J.; Geldart, D. An Investigation into Slugging Fluidized Beds. *Chem. Eng. Sci.* **1974**, *29*, 255.
- (31) Shaul, S.; Rabinovich, E.; Kalman, H. Generalized Flow Regime Diagram of Fluidized Beds Based on the Height to Bed Diameter Ratio. *Powder Technol.* **2012**, *228*, 264.
- (32) Ho, T. C.; Yutani, N.; Fan, L. T.; Walawender, W. P. The Onset of Slugging in Gas Fluidized Beds with Large Particles. *Powder Technol.* **1983**, *35*, 249.
- (33) Broadhurst, T. E.; Becker, H. A. Onset of Fluidization and Slugging in Beds of Uniform Particles. *AIChE J.* **1975**, *21*, 238.
- (34) Dimattia, D. G.; Amyotte, P. R.; Hamdullahpur, F. Slugging Characteristics of Group D Particles in Fluidized Beds. *Can. J. Chem. Eng.* **1997**, *75*, 452.
- (35) Singh, R. K.; Roy, G. K. Prediction of Minimum Slugging Velocity, Bubbling Bed Index and Range of Bubbling Fluidization in Cylindrical and Non-cylindrical Gas-solid Fluidized Beds. *Indian J. Chem. Technol.* **2008**, *15*, 85.
- (36) Singh, R. K.; Roy, G. K. Prediction of Minimum Bubbling Velocity, Fluidization Index and Range of Particulate Fluidization for Gas-solid Fluidization in Cylindrical and Non-cylindrical Beds. *Powder Technol.* **2005**, *159*, 168.
- (37) Wen, C. Y.; Yu, Y. H. A Generalized Method for Predicting the Minimum Fluidization Velocity. *AIChE J.* **1966**, *12*, 610.